A combined physicochemical-microstructural approach to predict the crack path at the topside interconnections in IGBT power devices

Microelectronics Reliability 132 (2022) 114516

Contents lists available at ScienceDirect

Microelectronics Reliability

journal homepage: www.elsevier.com/locate/microrel

A combined physicochemical-microstructural approach to predict the crack path at the topside interconnections in IGBT power devices

M. Shqair [a,*], Z. Khatir [a], A. Ibrahim [a], M. Berkani [b], A. Halouani [a], T. Hamieh [c]

[a] Gustave Eiffel University, Paris-Saclay Univ., ENS Paris-Saclay, CNRS, SATIE, 78000 Versailles, France
[b] Paris Est Créteil University, Paris-Saclay Univ., CNRS, SATIE, 91190 Gif-Sur-Yvette, France
[c] Faculty of Science and Engineering, Maastricht University, P.O. Box 616, 6200 MD Maastricht, the Netherlands

ARTICLE INFO

Keywords:
Semiconductor
Physicochemical-microstructural
Critical energy
Critical stress
Crack propagation

ABSTRACT

The thermal fatigue of the bond-wire contacts at the topside interconnections of power electronic devices is one of the main reliability issues. This paper presents a new methodological approach to characterize and model the damages during aging by a combination of fracture mechanics and physicochemical approaches. The approach relies first on correlating the change of the microstructure with aging at the bond-wire contact, then on looking for possible links between the microstructure and the parameters of damage models. After reviewing the effect of the microstructure on the whole cycling process, the correlation is made by relating the driving force of the device failure which is the crack propagation to some physicochemical properties and microstructural parameters such as surface energy (γ_s), grain boundary energy (γ_{gb}), misorientation angle between neighbor grains ($\Delta\theta$), plane of orientation of each singular grain, grain size and hardness values (H). This requires EBSD analysis and some post treatments. Those relationships were then used to configure the effect of the microstructure on cracks passage at the interconnection interfaces using cohesive zone models (CZM).

1. Introduction

Thermal fatigue is the driving force of the degradation of topside interconnection compartments of power electronic modules, traditionally made up of aluminum wires bonded on thin pads of aluminum films. It is the result of a large mismatch in the thermal expansion coefficients of silicon and aluminum present in semiconductor power devices such as MOSFETs and IGBTs.

Power modules based on IGBT chips (see Fig. 1) are the most used devices for energy conversion, having high efficiency and fast switching, in addition to the ability of their usage for high current and voltage applications [1]. During operative life, temperature variations due to power cycling lead to the formation of stresses and plastic deformations, which modify the microstructure of the materials at the interconnection interfaces of upper metallic parts. Wires and metallization layers become a lot more distorted with temperature than silicon layers, leading to the formation of continuous tensile and compressive stresses with different deformations. This affects on the material performance and leads to its degradation.

Thermal fatigue is divided into three consecutive stages, which are the initiation of micro-cracks, their transformation to macro-cracks, and the last stage which occurs when the degraded material cannot support loads anymore, resulting fast and sudden fracture [2]. Thus, fatigue problem is modeled by interpreting the crack formation and propagation.

As a first approximation, the microstructure of metals is made up of grains intersecting at grain boundaries. The grain is a region where atoms align, it is the unit cell of polycrystalline structures, whereas the grain boundary is a planar defect which separates those grains, it is the location of stress concentrations. This is the case of bonding wires and metallization layers.

Traditionally, the fatigue problem of electronic power modules is modeled by using coupled multiphysics (electrical, thermal and mechanical) finite elements models [3]. Some physicochemical studies were made previously to interpret the fatigue problem of metallic structures but only in the case of annealing at high and steady state temperatures, near melting points of the materials [4]. These conditions are totally different from the case of power semiconductor devices.

Recently, the influence of the microstructure and physicochemical properties on degradation processes has been the interest of several

* Corresponding author.
E-mail addresses: mustafa.shqair@univ-eiffel.fr (M. Shqair), zoubir.khatir@univ-eiffel.fr (Z. Khatir), ali.ibrahim@univ-eiffel.fr (A. Ibrahim), mounira.berkani@ens-paris-saclay.fr (M. Berkani), ayda.halouani@univ-eiffel.fr (A. Halouani), t.hamieh@maastrichtuniversity.nl (T. Hamieh).

https://doi.org/10.1016/j.microrel.2022.114516
Received 29 October 2021; Received in revised form 10 March 2022; Accepted 14 March 2022
Available online 29 March 2022

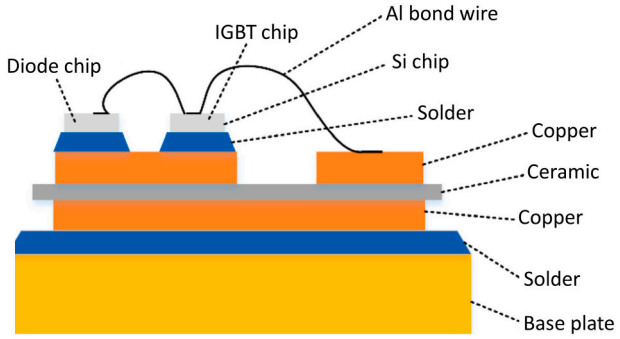

Fig. 1. Typical schematic assembly of IGBT power module.

scientists [5–8]. The effect of bonding procedures on the microstructure of the wire-metallization interconnection zone and its influence on materials reliability have been discussed by Broll et al. [9]. The effect of the wire bonding temperatures on cracks formation upon cycling has been investigated by Loh et al. [10]. The effect of the purity of materials on the evolution of their properties such as hardness and grain size upon cycling has been described by Agyakwa et al. [11]. The crack propagation pathway has been related to metallization reconstructions by Pederson et al. [12]. Last but not least, Zhou et al. [13] showed the effect of the evolution of grain sizes and misorientation angles on the crack growth, by which the rate of crack propagation decreases when the grain size decreases and the misorientation angle between neighbor grains increases.

Nowadays, one of the most used approaches for decohesion modeling to predict the crack propagation is based on cohesive zone models (CZMs) [14]. The CZM is a finite element multi-physics model for fracture mechanics, by which the fracture formation is regarded as gradual separation of intersecting surfaces. In CZMs, cracks formation and propagation are related to tractions and cohesion energies. In this paper, the work is concentrated on relating some physicochemical properties and microstructural features with the CZM parameters. Thus, the new approach proposed here is based on a combination between fracture mechanics and physicochemical-microstructural concepts. The goal of this new model is to predict the crack passage at interconnection interfaces between metallization layers and bonded wires from a physicochemical-microstructural point of view. Finally, this model is confronted with experimental observations.

2. The methodological approach

Thermal fatigue aging experiments in connection with the work presented in this paper are detailed in [15]. The analyzed IGBT power devices were SKIM63 manufactured by Semikron. Their mode of degradation is well described there.

As mentioned before, the fatigue problem is related to cracks formation and propagation. The goal of this work is to find relationships between the driving force of failure, i.e. the crack propagation from one side and microstructural features and physicochemical properties from the other side. These relations must relate the CZM parameters: a) the critical fracture energy density for separation (critical energy) and b) the maximal contact stress (critical stress), to microstructural characterization parameters such as: i) the misorientation angle between neighbor grains, ii) the plane of orientation of grains, iii) the size of grains, in addition to some physicochemical parameters such as the iv) surface energy, v) grain boundary energy and vi) hardness.

For this purpose, Electron Backscatter Diffraction (EBSD) and nanoindentation analysis for non-degraded IGBT sample have been performed. The CZM parameters are then deduced from this microstructural analysis by using known relationships and a program called ATEX [16].

Then, in order to simulate the crack propagation and predict the preferred crack path inside the microstructure, grains were represented by hexagons, where CZM elements were implemented at their boundaries. The geometry of hexagons was inspired from the honeycomb geometry, which is thought to be a good representative shape for grains. Hexagon's geometry is chosen because grains do not have specific shapes. Additionally, hexagons offer curvatures at the edges center, this looks closer to the shape of grains. Moreover, this geometry is flexible to control, by which critical energies and stresses can be inserted on their edges. In this way, the granular decohesion can be simulated by investigating the effects of microstructural parameters (grain size, grain boundaries misorientations…) on cracks formation through the parameters of local CZMs.

In the last step, the results of those simulations were compared with some scanning electron microscopy (SEM) experimental data for degraded IGBT samples, so that to validate the coherence between the simulations results and the experimental ones.

3. Calculating the CZM parameters

In order to predict the crack propagation physico-chemically and microstructurally, relationships between CZM parameters and physicochemical-microstructural features are required. Obtaining both CZM parameters was then achieved by a combination of physicochemical-microstructural equations and experimental data from EBSD and nanoindentation analysis. This section explains the strategy of calculating the critical energy and critical stress.

3.1. The critical energy needed for crack formation

The factor corresponding to the critical energy needed for cracks formation is the work of separation of two intersecting surfaces (W_{sep}). This parameter is the best representative parameter of the critical energy for the case of debonding between intersecting grains. At the microstructural scale, grains are the intersecting surfaces and their intersection regions are the grain boundaries. Eq. (1) below reflects this concept, where the work of separation is related to the surface energy of each grain (γ_s) and their grain boundary energy (γ_{gb}) [17,18]. These parameters are represented in (Fig. 2).

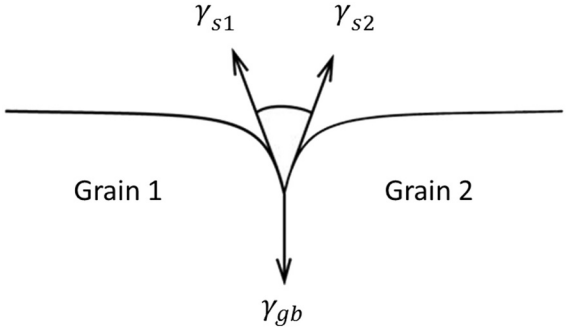

Fig. 2. Two neighbor grains and their grain boundary energy and individual surface energies schematization.

$$W_{sep} = \gamma_{s1} + \gamma_{s2} - \gamma_{gb} \quad (1)$$

The effect of temperature on fracture energy values will be considered indirectly through the microstructural changes that take place upon cycling, changing orientation planes, orientation angles and misorientation angles. Such changes affect on γ_s and γ_{gb} values, therefore W_{sep} changes. Additionally, since the maximum temperature reached upon cycling is only about 180 °C (≈0.27 of the melting point of aluminum),

thus we are working in the cold phase, and therefore the temperature will have a minor influence on the energy values [19]. The effect of cycling on the degradation processes is the dominant.

In order to calculate W_{sep}, we should know γ_s and γ_{gb}. For that, combinations were made between some equations from literature in the basis of EBSD analysis.

Fig. 3 is an EBSD image for a non-degraded IGBT sample at the interconnection contact between the wire and the metallization layer, indicating both wire edges positions (tip and heel). This sample was used to extract all the necessary data for obtaining the value of W_{sep} as mentioned previously.

Experimental observations show that cracks propagate from the interconnection edges (heel and tip). They continue growing from both edges toward the center until they meet when total fracture occurs [20]. In order to simplify our approach, the methodology of calculating the critical energy has been applied at the heel position.

Li et al. proposed some relationships as follows in Eqs. (2a), (2b) and (2c) for calculating the grain boundary energy in three different situations, depending on the misorientation angle between neighbor grains [21].

$$0^\circ < \Delta\theta < \theta_1; \gamma_{gb} = k\Delta\theta/\theta_1 \quad (2a)$$

$$\theta_1 < \Delta\theta < \theta_2; \gamma_{gb} = k \quad (2b)$$

$$\theta_2 < \Delta\theta < 90^\circ; \gamma_{gb} = k\,(90\text{–}\Delta\theta)/(90\text{–}\theta_2) \quad (2c)$$

where $\Delta\theta$ is the misorientation angle between grains, k is the Hall-Petch constant (0.6 J/m^2 for aluminum [21]) and θ_1 and θ_2 are specific angles, where $\theta_1 = 20^\circ$ and $\theta_2 = 70^\circ$ in the case of polycrystalline aluminum [22].

The ATEX software was used to calculate the grain boundary energies by obtaining the necessary microstructural parameter, which are the misorientation angles between neighbor grains. Fig. 4 shows the crystal orientation of each grain at the heel position. Each of these oriented crystals has its own Euler indices representing the angles of orientations in all directions as seen for the grain indicated by the red arrow. Having such a difference in orientation angles among grains leads to different misorientation angle values. Fig. 5 shows the misorientation angles between neighbor grains. From the data of both figures, the grain boundary energy can be calculated using Eqs. (2a), (2b) and (2c).

From Fig. 4 it is seen that the orientation angle between neighbor grains highly differs from one grain to another. From Fig. 5 it is observed that low boundary angles are dominant above the interconnection interface. Thus, boundary energies are mainly low for major boundaries referring to Eq. (2a) used for calculating the boundary energy for the case of low misorientation angles. In this condition, and referring to Eq. (1), the resulting cohesive energies are high. In contrary, when looking at the grains just at the interconnection sites, it is observed that the number of boundaries owing higher misorientation angles is higher, thus the boundary energies here are generally greater referring to Eqs. (2b) and (2c), therefore the cohesion energies are lower from Eq. (1).

The remaining parameter needed to calculate the cohesive energy is the surface energy. From literature, the values of surface energies of aluminum are mainly dependent on the plane of orientation of each grain [23]. Each plane of orientation has its own surface energy as summarized in Table 1.

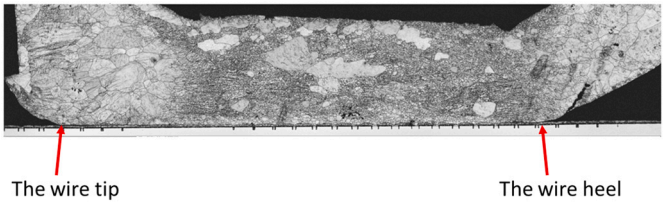

Fig. 3. EBSD image of a non-degraded IGBT sample (SKIM63 module) at the interconnection between the wire and the metallization layer.

It is observed that the values of surface energy are greater than grain boundary energy values. For determining the surface energy values, it is necessary to have the plane of orientations of grains. For this purpose, Inverse Pole Figures (IFPs) are plotted in directions X, Y and Z as seen in Fig. 6.

By looking at X, Y and Z directions, it is seen that for each direction there is a favorable grain orientation for grains at the interconnection zone and for grains in the wire bulk. Referring back to Eq. (1), the work of separation values representing the cohesive energies are calculated. Cohesive energies between grains vary between 0.65 and 1.8 J/m^2.

3.2. The critical stress needed for crack formation

The critical stress is the second CZM parameter needed to model the crack formation. Its value is affected by the grain size since it is linked to yield strength according to Hall-Petch equation (Eq. (3)) [24], where the yield stress is inversely proportional to the grain size:

$$\sigma_y = \sigma_0 + k_{HP}\, d^{-0.5} \quad (3)$$

In this relation, d is the grain size, σ_y is the yield stress, σ_0 is the friction stress (constant) and k_{HP} is the Hall-Petch constant.

In order to calculate the values of the maximal contact stress, we should find a linkage between this mechanical parameter and physicochemical properties. Since this factor has a pure mechanical concept, the closest parameter to it is the tensile stress when taking the normal direction. This approximation was also seen in the ANSYS verification manual [25]. Tensile stress is a more flexible parameter, where some physicochemical features can be linked to it. Thus, in this work, the tensile stress will be used as a representative parameter of the critical stress in order to relate it to some physicochemical properties.

From references [26,27] the relations between yield stress, hardness (H) and tensile stress (σ_{TS}) are listed in Eqs. (4) and (5) below, where (n) is the strain hardening exponent.

$$\sigma_y = \frac{H}{3}\, 0.1^n \quad (4)$$

$$\sigma_{TS} = \frac{H}{2.9}\left(\frac{n}{0.217}\right)^n \quad (5)$$

By combining these two relations, and by eliminating the hardness H, one can link the tensile stress and the yield stress:

$$\sigma_{TS} \approx 1.03\, \sigma_y\, (46.1\, n)^n \quad (6)$$

Even though the hardness measurements were operated through nanoindentation tests, the probable existence of certain amount of impurities upon bonding the wire makes it difficult to know precisely the values of yield and tensile stresses theoretically, since the strain hardening values for each grain will not be accurately known. Moreover, the hardness measurements were not precisely done at the wire edges since the thickness of the wire is very small at those positions after the welding process, thus our nanoindentation data may not be highly accurate because the hardness values are highly local. For this reason, additional method was used to obtain the tensile strength values inside the wire from yield stress and hardness values in the upcoming step.

The strength values for grains inside the metallization are close since all grains are small with approximately the same size. The case is different for the grains inside the wire, where we cannot assume close values of strength for grains inside the wire. This is because the grain sizes are highly random inside the wire, by which it is possible to have very big grains and very small grains in the same sample.

Starting with the yield stress, we find in the literature that for aluminum thin films such as metallization layers, the values are mainly between 100 and 150 MPa [28]. For aluminum wires, the values are between 10 and 30 MPa [29]. The strain hardening exponent is reported

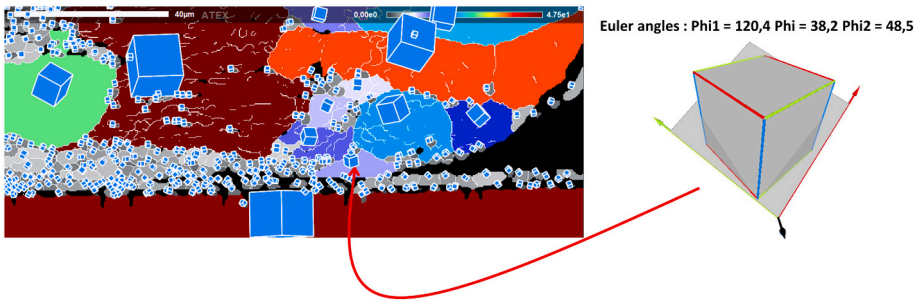

Fig. 4. Grains orientations and Euler indices representing their orientation angles at the heel position.

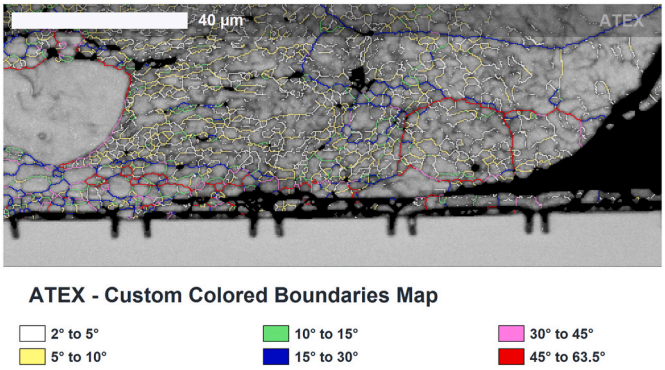

Fig. 5. Misorientation angles between grains at the heel position.

Table 1
Values of aluminum surface energies for different orientations (100), (110) and (111) calculated according to [23].

Plane of orientation	Surface energy (J/m^2)
(100)	0.900
(110)	0.972
(111)	0.620

in literature in the range of 0.05–0.2 [30].

Concerning the tensile strength values which represent the critical stresses for debonding in the CZM, these values are about 175 MPa for the grains at the metallization layer. This can be deduced when looking at the tensile stress values with different film thicknesses and the ratio of these tensile stress values to their corresponding yield stress as reported in reference [31]. This value could be also concluded as an average upon using Eq. (6). For obtaining the tensile stress values for the grains inside the wire, a relationship was established between hardness values and tensile stress values [32]. This article was working on aluminum wires in MOSFETs, with doing the same nanoindentation procedure to obtain the hardness values. When comparing the hardness values obtained in this article at the metallic interconnection sites with our values, big compatibility was observed, where the values are ranging between 450 and 550 MPa. In that paper, the corresponding tensile stress values for these hardness values are ranging between 80 and 120 MPa. This variation in values is due to the local characteristics of grains such as the grain size, where smaller grains acquire higher strength. These values can be used as average tensile stress values inside the wire at the interconnection zone in our model.

4. Two dimensional ANSYS modeling of the crack path

In the basis of the previous analysis, a finite element model has been made in order to evaluate the approach and to compare it with experimental observations. The power module used in this study is a multichip IGBT power module (SKIM63), but only a simplified representation in 2D of a single chip has been modeled for simplification reasons. The

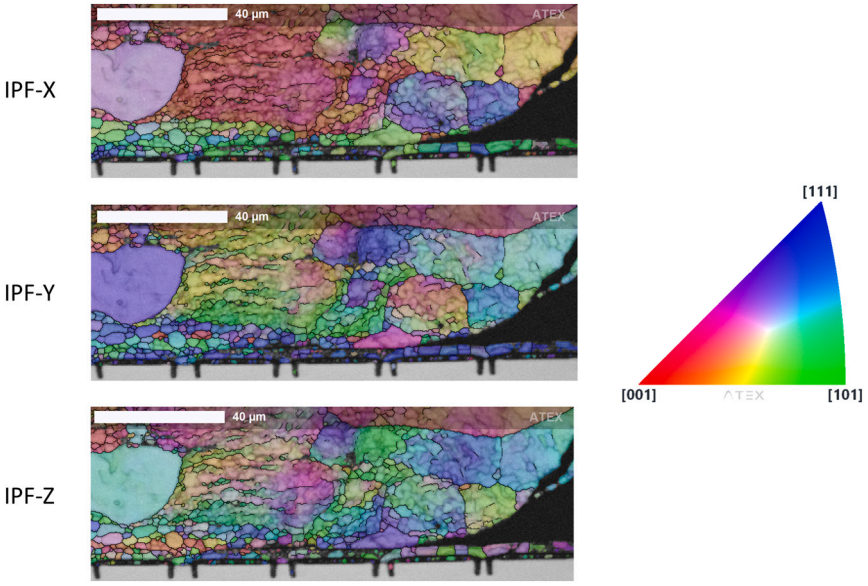

Fig. 6. IFPs in directions X, Y and Z to get the plane of orientations of grains at the heel position.

Table 2
The dimensions of the power assembly model.

Material	Length (mm)	Width (μm)
Aluminum wire (Al)	13.9	380
Metallization layer (Al)	6.2	5
Silicon (Si)	7.7	140
Silver (Ag)	7.7	20
Superior copper (Cu)	36	300
Ceramic (Al_2O_3)	39	380
Inferior copper (Cu)	36	300
Superior thermal interface (TIM)	38	100
Aluminum plate (Al)	170	5000
Inferior thermal interface (TIM)	170	100
The cooling system (Al)	170	10,000

Table 3
Material properties of SKIM63 module components.

	Al	Si	Ag	Cu	Al_2O_3	TIM
Density (kg/m^3)	2700	2330	7350	8960	3780	–
Electric resist. (Ω·m)	2.7e−8	$R_x >>> R_y$	4e−8	1.7e−8	1e12	1e20
Thermal conduc. (W/m·K)	238	124	250	390	24	2
Thermal capacity (J/kg·K)	897	750	230	390	830	–
Poisson ratio	0.33	0.3	0.37	0.34	0.2	0.33
CTE (ppm/K)	23.5	4.1	19.6	17	8	23.5
Young modulus (GPa)	76	131	6.28	97	370	76

dimensions used for the geometrical model are given in Table 2. The material properties for the IGBT compartments are listed in Table 3. The non-linear mechanical properties of the metallization's and wire's aluminum in addition to copper are presented in Fig. 7 [29,33].

Grains seen in Figs. 4, 5 and 6 at the heel position are represented by hexagons and positioned at the interconnection interface. In this model, each hexagon was supposed to have a radius equals to 3.54 μm, where this size is close to the size of a grain in the reality. Even if the cell sizes are identical in the geometrical model, we can account for different sizes and misorientation angles by using localized CZM parameters in accordance with the characteristics of the local microstructure. Since the objective is to simulate the behavior and the preferential path of the crack at the beginning of crack propagation, the cell network has been limited to the heel edge position. Sixty-one hexagons were put at the heel position as seen in Fig. 8.

Since grains have different sizes especially inside the wire, it was assumed that there are three different grain size zones, where zone 1 is for the grains inside the metallization, zone 2 is for grains in the wire just at the interconnection with metallization, and zone 3 is for grains above the grains in zone 2. This can be clearly seen in Fig. 9 representing the grains at the heel position.

After showing the existence of the three grain size zones, these zones were considered to exist in the hexagons inserted in the simulations, in order to model very roughly the particle size existing in the microstructure. The first zone which is inside the metallization was assumed to have hexagons of 3 μm size, zone 2 inside the wire at the contact interface acquires bigger sizes (3.5 μm), and finally a zone 3 inside the wire above zone 2 with reduced sizes (2 μm). These three different zones are represented in Fig. 10. The effect of having different sizes values will be reflected on the values of strength they acquire.

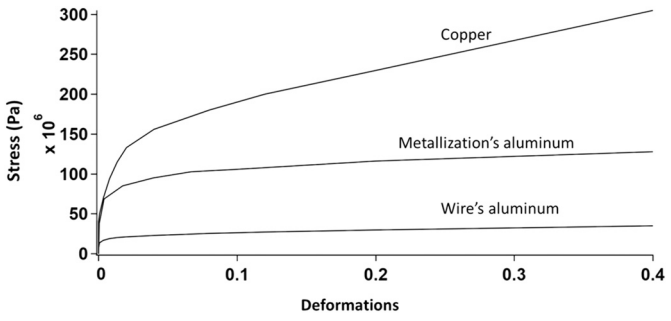

Fig. 7. Elastoplastic stress–strain behaviors for aluminum and copper.

For the metallization layer (zone 1), it has higher strength than the strength of the wire as mentioned previously. This is because the wires are thick, having very big grains at the upside positions and very small sizes near the interconnection, whereas metallization layers are thin films with no big variations in grain sizes they have. Additionally, the composition of the metallization layer and the wire are not exactly the same by looking at the percentages of impurities in both compartments. Moreover, it was assumed that zone 3 has higher critical energy values since the misorientation angles are lower than those in zone 2 as observed in Fig. 5. This results higher critical energy values as discussed previously.

Bilinear mixed-mode CZMs from the ANSYS software have been applied, where critical normal and tangential stresses and fracture energies were put at each edge of the hexagon cells of Fig. 10. Such a model is proposed by Alfano and Crisfiled, by which it can reflect cyclic degradation by linearly reducing stiffness through using a reduction factor $(1 - d_n)$, where d_n is cumulative damage after n loadings ($0 \leq d_n \leq 1$). If $d_n = 1$, debonding is total [34]. For reasons of simplification, it is assumed that critical stresses and energies have the same values in both directions, normal and tangential. Thus, tensile stress values representing the critical normal stress values for crack formation as mentioned previously are used for both directions.

Critical stresses values are high in reality compared to the generated stresses in the simulation at early cycling, therefore, these values are divided by a factor of 2.75 for the hexagons inside the wire in order to speed up the debonding and to see the crack formation from the first cycles. For the metallization layer the values are divided by a smaller factor which is 2.25, because when putting high factors such as 2.75, debonding inside the metallization will be dominant. The reason is that higher stresses are generated inside the metallization layer than that in the wire, however in the same time the debonding inside the metallization not inside the wire is illogical since the real tensile strengths for the metallization grains are surely higher than that for the wire grains. Then, for zones 1, 2 and 3, the normal and tangential critical stresses are set to be 78 MPa (175/2.25), 28 MPa (80/2.75) and 40 MPa (110/2.75) respectively, whereas the normal and tangential critical energies are set to be 1 J/m^2, 1 J/m^2 and 1.8 J/m^2 respectively for all the hexagon edges.

Additional cause for using specifically the 28 MPa and 40 MPa reduced critical stress values can be mentioned here. By assuming the 28 MPa value for hexagons in zone 2, the yield strength for those hexagons can be deduced using Eq. (6). It is assumed that the hexagons size in zone 2 (d_2) is about 3,5 μm and about 2 μm for the hexagons in zone 3 (d_3), and the strain hardening coefficient (n) = 0.1. By subtracting the Hall-Petch equations corresponding to both zones, the yield strength value for the hexagons in zone 3 can be deduced after knowing by how much the yield strength value for hexagons in zone 3 is greater than that for hexagons in zone 2. Finally, using Eq. (6), the 40 MPa for zone 3 is obtained.

As the mechanical behavior does not have significant feedbacks on the thermal results, a weak thermo-mechanical coupling has been chosen in the simulation model. Thus, two consecutive simulations were applied to represent the power cycling. The first one is an electro-thermal simulation for the whole system to obtain the most representative possible thermal gradients. Then, the resulting temperature maps are used as loads for a mechanical simulation associated with the mixed-mode CZM. Since the computation time is high, only few cycles can be reasonably simulated in order to see the first occurring processes and the initial crack propagation path.

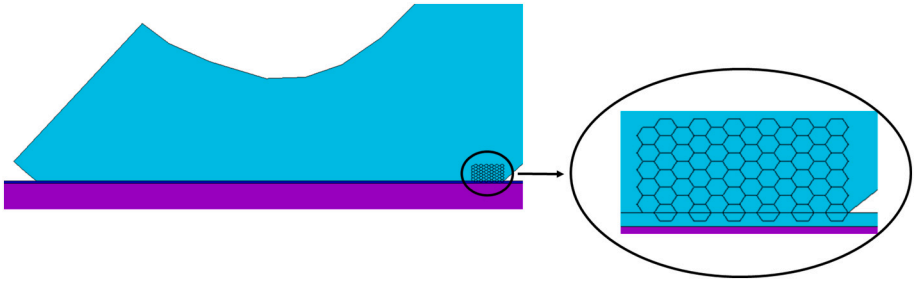

Fig. 8. Hexagons representing the grains at the contact between the bond-wire and the metallization layer at the heel position.

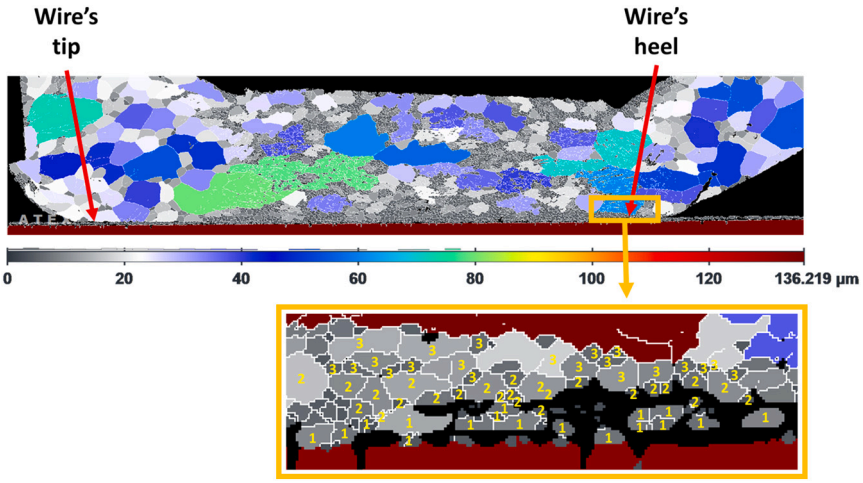

Fig. 9. Grains numbered 1, 2 and 3 representing the three different grain size zones at the heel position.

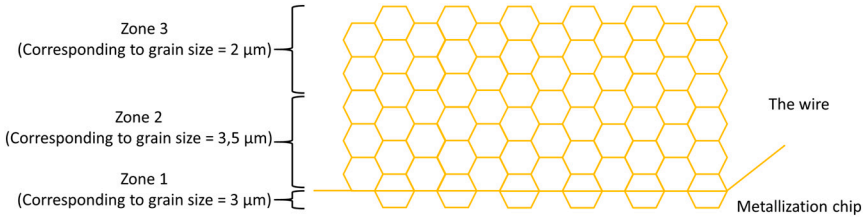

Fig. 10. The three hexagon layers representing the three grain size zones in Fig. 9.

4.1. Electro-thermal simulation

Concerning the electro-thermal simulation, eight power cycles (ON/OFF states) in a DC mode were applied. As for the experimental tests described in [15], during the heating phase a current density of 7337 A/m^2 was injected in the device during 3 s (t_{ON}) corresponding to 56.5 A. This leads to a forward voltage through the IGBT chip of approximately 2 V. The cooling phase was considered to have a duration of 6 s (t_{OFF}). The cooling model is represented by a forced convection at the bottom part of the module with a convection coefficient of 1500 W/m^2·K and an ambient temperature of 45 °C. These test conditions led to a junction temperature swing of $\Delta T_j = 110$ ° C due to Joule effect. This junction temperature swing value was specifically chosen since it corresponds to the experimental test conditions in [15]. Fig. 11 shows the initial and boundary conditions of this electro-thermal simulation.

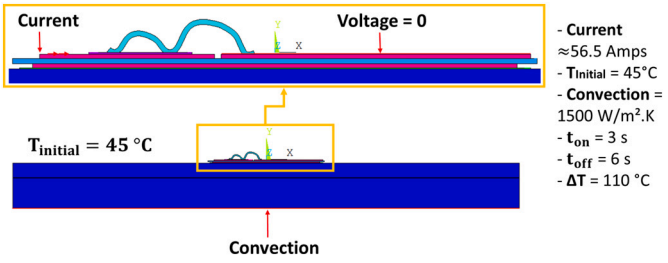

Fig. 11. The electrical simulation boundary conditions.

4.2. Mechanical simulation

The temperature maps obtained by the electro-thermal simulation were used as loads for the mechanical one. Since major deformations occur at the upper metallic part, only those parts are considered in this simulation. Zero-displacement boundary conditions were applied at the bottom edges of the lower copper layer (lower DCB part) as seen in Fig. 12. In addition, all the hexagon edges were assigned as contact pairs associated with CZM parameters as mentioned previously to see the crack formation and propagation. Those inserted parameters were controlling the debonding process (cracks formation) according to the generated stresses.

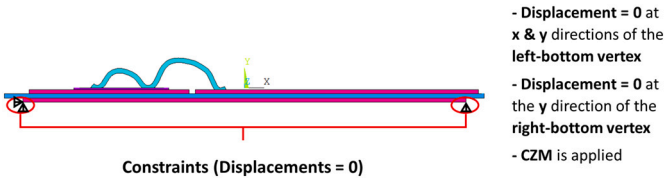

Fig. 12. The mechanical constraints applied on the edges of the lower part of the DCB substrate.

5. Simulations results

The resulting junction temperature swing averaged on the volume of the IGBT chip, can be seen in Fig. 13.

Normal stresses σ_x, σ_y and shear stresses σ_{xy} are plotted at the end of the eighth cycle for the three zones in Figs. 14, 15 and 16 respectively (unit is Pa). These stresses values are plotted in order to compare them with the CZM stresses values. When normal or tangential stresses are greater than the normal or tangential CZM parameters, debonding is expected to occur. For debonded contact pairs the values of stresses decrease until reaching a value of zero when debonding is complete.

From previous figures, it can be concluded that debonding is expected to occur mainly in zone 2 since stresses values in some positions in this zone exceeded the critical stresses, in addition, stresses there are generally higher than those in zone 3. Moreover, hexagons in zone 1 have much higher strength than those in zones 2 and 3. In order to verify this, Fig. 17 showing the debonding map after 8 power cycles at the heel position was plotted. In this figure, the scale is the debonding factor, which ranges from 0 (no debonding) to 1(full debonding). Intermediate values give locations with partial debonding.

By applying the same simulations with all previous conditions but this time by inserting the sixty-one hexagons at the tip position not at the heel one, the crack formation was slower, this maybe signifies that cracks start formation primarily at the heel position and then after several number of cycles other cracks start to form at the tip position. The debonding map at the tip position is plotted in Fig. 18.

Starting from what was mentioned in the previous sections about the crack propagation dependence on physicochemical-microstructural parameters through linking them to the CZM parameters, other things can be also concluded from the debonding maps. First, debonding is observed to be at the zone just above the interconnection between the wire and the metallization. This is logical since the generated stresses are higher than their corresponding critical fracture stresses. Debonding did not occur inside the metallization layer even though the generated stresses are high, this is because all the grains of thin metallization films have small grain sizes, thus they acquire higher strength referring to the Hall-Petch relationship, therefore their corresponding critical stress for debonding are higher. The situation inside the wire is totally different, where grains are generally larger and it is possible to have high variety in terms of grain size between one grain and its neighbor. Additionally,

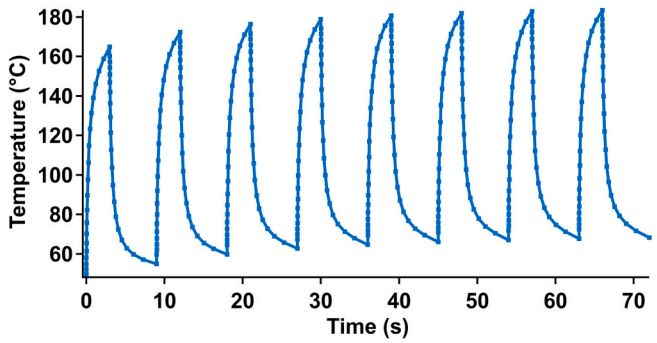

Fig. 13. Junction temperature profile after 8 power cycles.

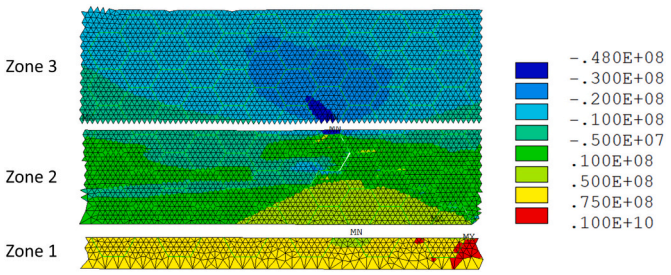

Fig. 14. σ_x distribution at the heel position in zones 1, 2 and 3.

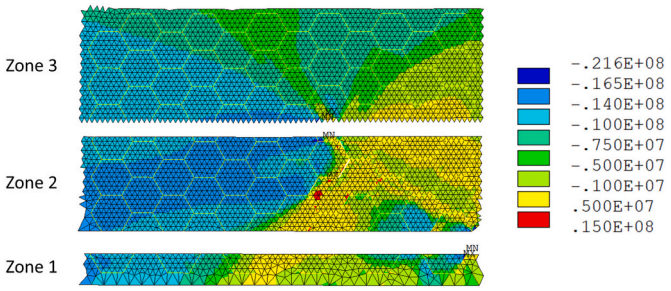

Fig. 15. σ_{xy} distribution at the heel position in zones 1, 2 and 3.

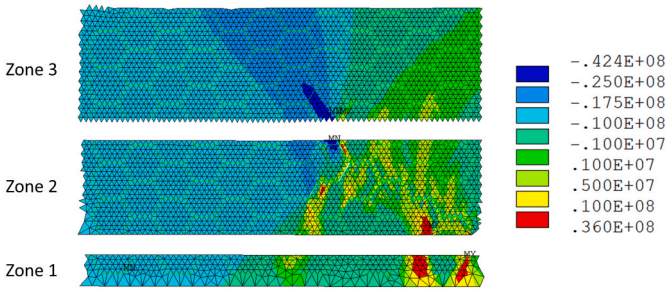

Fig. 16. σ_y distribution at the heel position in zones 1, 2 and 3.

from the simulations results it was deduced that debonding starts from terminal hexagons at the interconnection between the bonded wire and the metallization layer at both heel and tip positions. This is due to the existence of maximal temperatures and stresses at those positions. Moreover, it is deduced that cracks start formation at heel position with higher speed than that at the tip.

Experimentally from SEM, cracking just above the interconnection interface was verified. Fig. 19 shows the crack evolution at different number of cycles. From this figure, it is deduced that cracks are formed first at the heel position with faster speed than that at the tip. This can be realized when comparing the wire's crack path at both wire's tip and heel positions for samples degraded at 10% and 25% N_f, where N_f is the number of cycles to failure. Cracks then continue propagating from both edges toward the center of the bottom wire zone, as observed in the sample degraded at 50% N_f. When N_f is reached (100% N_f), cracks are totally distributed at the whole bottom wire zone, where total separation (lift off) occurs. All these observations are in coherence with literature and experimental data [10,11].

6. Conclusions

This paper showed a new approach of modeling the fatigue problem of the upper part of semiconductor power electronics, by relating it to several physicochemical and microstructural parameters, such as the grain boundary energy, surface energy, grain size, the misorientation

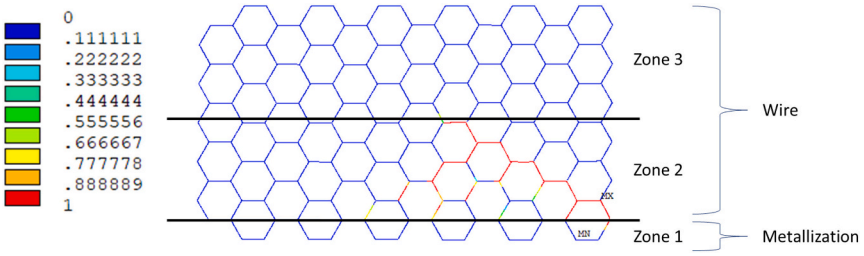

Fig. 17. Debonding map at the heel position after 8 power cycles.

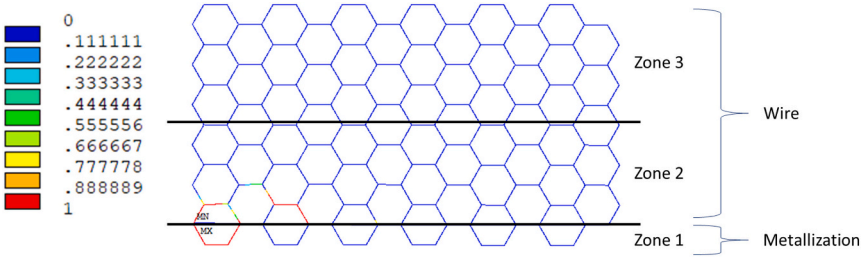

Fig. 18. Debonding map at the tip position after 8 power cycles.

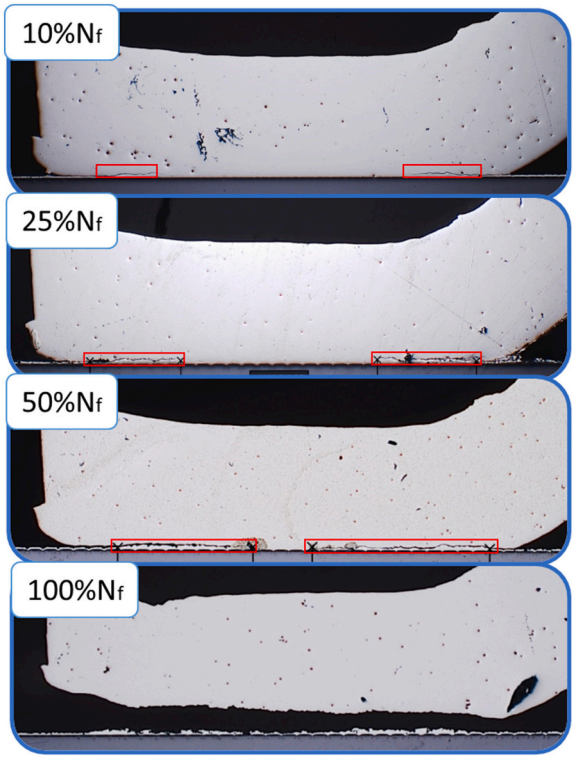

Fig. 19. The crack propagation for samples degraded at 10% N_f, 25% N_f, 50% N_f and 100% N_f.

angle and hardness. The relationships between those parameters and the crack formation and propagation processes, in addition to the possibility to predict the crack formation and propagation from physicochemical-microstructural factors have been shown in the second section. Those relationships were expressed in the third section by modeling the fatigue problem using the ANSYS program, where the effect of physicochemical-microstructural factors was so clear on the debonding and cracks formation. Cracks were seen to occur near the wire-metallization interconnection starting from the wire edges, most probably from the heel position. This was verified experimentally from SEM tests, after showing some degraded samples. All these degradation observations were shown to be related to microstructural features and physicochemical properties of degraded materials. Such study has the advantage of enabling us to understand smoothly the manner of crack formation and the main parameters affecting on it through interpreting the microstructural changes occurring.

CRediT authorship contribution statement

Mustafa Shqair: Conceptualization, Methodology, Software, Writing - Original draft preparation. Zoubir Khatir: Supervision, Conceptualization, Validation, Writing - Review & editing. Ali Ibrahim: Supervision, Conceptualization, Writing - Review & editing. Mounira Berkani: Conceptualization. Ayda Halouani: Writing - Reviewing and editing. Tayssir Hamieh: Writing - Reviewing and editing.

Declaration of competing interest

The authors declare that they have no known competing financial interests or personal relationships that could have appeared to influence the work reported in this paper.

References

[1] H.K. Tseng, M.L. Wu, Electro-thermal-mechanical modeling of wire bonding failures in IGBT, in: Proc. Tech. Pap. - Int. Microsystems, Packag. Assem. Circuits Technol. Conf. IMPACT, 2013, pp. 152–157.
[2] R.G. Budynas, K. Nisbett, Shigley's Mechanical Engineering Design, 2008.
[3] H. Medjahed, P.E. Vidal, B. Nogarede, Thermo-mechanical stress of bonded wires used in high power modules with alternating and direct current modes, Microelectron. Reliab. 52 (2012) 1099–1104.
[4] W.W. Mullins, Theory of linear facet growth during thermal etching, Philos. Mag. 6 (1961) 1313–1341.
[5] G.P. Zhang, C.A. Volkert, R. Schwaiger, R. Mönig, O. Kraft, Fatigue and thermal fatigue damage analysis of thin metal films, Microelectron. Reliab. 47 (2007) 2007–2013.
[6] S. Zaefferer, J.C. Kuo, Z. Zhao, M. Winning, D. Raabe, On the influence of the grain boundary misorientation on the plastic deformation of aluminum bicrystals, Acta Mater. 51 (2003) 4719–4735.
[7] D. Martineau, C. Levade, M. Legros, P. Dupuy, T. Mazeaud, Universal mechanisms of Al metallization ageing in power MOSFET devices, Microelectron. Reliab. 54 (2014) 2432–2439.
[8] R. Ruffilli, Fatigue Mechanisms in Al-based Metallizations in Power MOSFETs, Université Paul Sabatier-Toulouse III, 2017. PhD diss.

[9] M.S. Broll, U. Geissler, J. Höfer, S. Schmitz, O. Wittler, K.D. Lang, Microstructural evolution of ultrasonic-bonded aluminum wires, Microelectron. Reliab. 55 (2015) 961–968.
[10] W. Loh, M. Corfield, H. Lu, S. Hogg, T. Tilford, C.M. Johnson, Wire bond reliability for power electronic modules - effect of bonding temperature, in: International Conference on Thermal, Mechanical and Multi-Physics Simulation Experiments in Microelectronics and Micro-Systems, 2007, p. 6.
[11] P.A. Agyakwa, L. Yang, E. Arjmand, P. Evans, M.R. Corfield, C.M. Johnson, Damage evolution in Al wire bonds subjected to a junction temperature fluctuation of 30 K, J. Electron. Mater. 45 (2016) 3659–3672.
[12] K.B. Pedersen, L.H. Østergaard, P.K. Kristensen, P. Ghimire, V.N. Popok, K. Pedersen, Degradation evolution in high power IGBT modules subjected to sinusoidal current load, J. Mater. Sci. Mater. Electron. 27 (2016) 1938–1945.
[13] P. Zhou, J. Zhou, Z. Ye, X. Hong, H. Huang, W. Xu, Effect of grain size and misorientation angle on fatigue crack growth of nanocrystalline materials, Mater. Sci. Eng. A 663 (2016) 1–7.
[14] G. Giuliese, A. Pirondi, F. Moroni, A cohesive zone model for three-dimensional fatigue debonding/delamination, Procedia Mater. Sci. 3 (2014) 1473–1478.
[15] N. Dornic, A. Ibrahim, Z. Khatir, N. Degrenne, S. Mollov, D. Ingrosso, Analysis of the aging mechanism occurring at the bond-wire contact of IGBT power devices during power cycling, Microelectron. Reliab. 114 (2020), 113873.
[16] B. Beausir, J.-J. Fundenberger, Analysis Tools for Electron And X-ray Diffraction, ATEX-software, Université de Lorraine, Metz, 2017.
[17] H. Zheng, et al., in: "Grain boundary properties of elemental metals," arXiv 186, 2019, pp. 40–49.
[18] J.J. Möller, E. Bitzek, Fracture toughness and bond trapping of grain boundary cracks, Acta Mater. 73 (2014) 1–11.
[19] Z. Wang, et al., Effects of finite temperature on the surface energy in Al alloys from first-principles calculations, Appl. Surf. Sci. 479 (2019) 499–505.
[20] S. Buhrkal-Donau, Comparative study of wire bond degradation under power and mechanical cycling tests, 2018.
[21] Z. Li, C. Hou, M. Huang, C. Ouyang, Strengthening mechanism in micro-polycrystals with penetrable grain boundaries by discrete dislocation dynamics simulation and Hall-Petch effect, Comput. Mater. Sci. 46 (2009) 1124–1134.
[22] G.C. Hasson, C. Goux, Interfacial energies of tilt boundaries in aluminium. Experimental and theoretical determination, Scr. Metall. 5 (1971) 889–894.
[23] J.M. Zhang, F. Ma, K.W. Xu, Calculation of the surface energy of FCC metals with modified embedded-atom method, Appl. Surf. Sci. 229 (2004) 34–42.
[24] R.W. Armstrong, The cleavage strength of pre-cracked polycrystals, Eng. Fract. Mech. 28 (1987) 529–538.
[25] ANSYS® Mechanical APDL 15.0, ANSYS Mechanical APDL Verification Manual, 2013.
[26] J.R. Cahoon, W.H. Broughton, A.R. Kutzak, The determination of yield strength from hardness measurements, Metall. Trans. 2 (1971) 1979–1983.
[27] J.R. Cahoon, An improved equation relating hardness to ultimate strength, Metall. Trans. 3 (1972) 3040.
[28] N. Tsuji, Y. Ito, Y. Saito, Y. Minamino, Strength and ductility of ultrafine grained aluminum and iron produced by ARB and annealing, Scr. Mater. 47 (2002) 893–899.
[29] Y. Nagatomo, T. Nagase, S. Shimamura, FEM analysis of thermal cycle properties of the substrates for power modules, J. Jpn. Inst. Electron. Packag. 3 (2000) 330–334.
[30] S. Kalpakjian, S. Schmid, Mechanical behavior, testing, and manufacturing properties of materials, in: ManufacturingEngineering & Technology, 2010, pp. 56–87.
[31] H. Kubo, M. Ciappa, T. Masunaga, W. Fichtner, Multiscale simulation of aluminum thin films for the design of highly-reliable MEMS devices, Microelectron. Reliab. 49 (2009) 1278–1282.
[32] M.S. Broll, et al., Correlation between mechanical properties and microstructure of different aluminum wire qualities after ultrasonic bonding, Microelectron. Reliab. 55 (2015) 1855–1860.
[33] J.F. Shackelford, W. Alexander, Materials Science and Engineering Handbook, Third Edition, CRC Press, 2000, p. 1928.
[34] G. Alfano, M.A. Crisfield, Finite element interface models for the delamination analysis of laminated composites: mechanical and computational issues, Int. J. Numer. Methods Eng. 50 (2001) 1701–1736.